DEEP CONVOLUTIONAL NEURAL NETWORKS-BASED SCATTERER DENSITY ESTIMATOR IN OPTICAL COHERENCE TOMOGRAPHY

THITIYA SEESAN

A THESIS SUBMITTED IN PARTIAL FULFILLMENT OF THE REQUIREMENT FOR THE DEGREE OF MASTER IN PHYSICS

DEPARTMENT OF PHYSICS SCHOOL OF SCIENCE

KING MONGKUT'S INSTITUTE OF TECHNOLOGY LADKRABANG

2021

KMITL-2021-SC-M-030-058

School of Science

King Mongkut's Institute of Technology Ladkrabang

Thesis Certification

Thesis Title Deep Convolutional Neural Networks-based Scatterer Density Estimator in Optical Coherence Tomography

Student Name Miss Thitiya Seesan

Student ID 61605075

Degree Master of Science (Applied Physics)

Department Physics

Thesis Advisor Asst. Prof. Dr. Prathan Buranasiri

Thesis Committee	Signatures
Asst. Prof. Dr. Suebtarkul Suchat Chairperson and Examiner	
Dr. Witoon Yindeesuk Examiner	
Asst. Prof. Dr. Prathan Buranasiri Examiner	

Examination Date 20th December 2021 **Time** 01.00 - 04.00 p.m.

Place Online Exam

Approved by School of Science

(Assoc. Prof. Dr. Sutee Chutipaijit)

Dean

Date 29th December 2021

Project Title	DEEP CONVOLUTIONAL NEURAL NETWORKS-BASED SCATTERER DENSITY ESTIMATOR IN OPTICAL COHERENCE TOMOGRAPHY
Student	THITIYA SEESAN
Student ID	61605075
Degree	Master of Science (Applied Physics)
Department	Physics
Year	2021
Advisor	Asst.Prof.Dr.Prathan Buranasiri

Abstract

We present deep convolutional neural network (DCNN)-based estimators of the tissue scatterer density, lateral and axial resolutions, signal-to-noise ratio, and effective number of scatterers (i.e., the number of scatterers within a resolution volume). The estimators analyze the speckle pattern of an optical coherence tomography (OCT) image in estimating these parameters. The DCNN is trained by a large number (1,280,000) of image patches that are fully numerically generated in OCT imaging simulation. Numerical and experimental validations were performed. The numerical validation shows good estimation accuracy. The experimental validation using scattering phantoms shows the reasonable estimations of the scatterer density and the resolutions. The scatterer density estimator was also applied to an *in vitro* tumor cell spheroid, and a reduction in the scatterer density during cell necrosis was found.

Acknowledgment

This thesis is based on the works which the author have attended to as a Master's student of Department of Physics, School of Science, King Mongkut's Institute of Technology Ladkrabang, Ladkrabang. This thesis would not have been possible without the kind help of many people.

First, I shall be grateful to my supervisor, Prof. Prathan Buranasiri. He provides me the best environment for research and is a good mentor. Thanks to School of Science, King Mongkut's Institute of Technology Ladkrabang, Ladkrabang for awarding me a Dissertation Completion Fellowship, providing me with the financial means to complete this project.

I would like to express my sincere gratitude to my supervisor in Japan Prof. Yoshiaki Yasuno, who is a principle investigator of Computational Optics Group (COG), University of Tsukuba, Japan, for your patience, guidance, and support. I have benefited greatly from your wealth of knowledge and meticulous editing. I am extremely grateful that you took me on as a student and continued to have faith in me over the years. I sincerely thank all of current COG members: Prof. Shuichi Makita, Dr. Arata Miyazazwa, Dr. Pradipta Mukherjee, Dr.Antonia Lichtenegger, Ibrahim Abd Ei-Sadek, Lida Zhu, Kensuke Oikawa, Kiriko Tomita, Rion Morishita, Jiajie Lou, Yiqiang Zhu, Yusong Liu, and Shumpei Kojima.

I would like thank to secretaries of COG: Tomomi Nakayama, Kayo Yuyama, and Yoko Furukawa. They have supported me for many times.

I would like to thank anonymous reviewers of the OCT community for their careful reading of our manuscript and their insightful comments and suggestions.

Finally I would like to thank my family. My parents and sister are not only patrons to get higher education, but also great supporter in my life.

THITIYA SEESAN

Content

List of Figures

List of Figures (Continue)

Figure **Page**

Chapter 1
Introduction

Speckle is an inevitable phenomenon in the image formation of optical coherence tomography (OCT) [1]. The speckle is an information carrier that conveys the properties of tissues, such as the sub-resolution distribution of the scatterers[2] and sub-resolution translation [3, 4]. In addition, speckle carries properties of the imaging system itself, such as the optical resolution[1]. We refer to these properties as "fundamental parameters" in this paper. This information-carrying nature of the speckle motivates us to measure/estimate the fundamental parameters through the speckle patterns of an OCT image.

However, the relationship between these parameters and the speckle pattern is complicated, and it is thus not straightforward to estimate these parameters from the OCT image. This complexity comes from the image formation process. In principle, OCT imaging processes can be understood as a combination of two sequential processes. The first process is a forward process in which the tissue property is encoded into an interference signal. The second process is the backward process in which the interference signal is processed to form an OCT image, and the OCT image is then analyzed to estimate the fundamental parameters. The principle is exemplified by attenuation coefficient estimation [5, 6, 7], signal intensity estimators[8, 9], and polarization parameter estimations of polarization sensitive OCT[10, 11, 12, 13, 14].

In general, the forward process is definitive and can be easily modeled, and also can be relatively easily numerically simulated [15, 16, 17]. On the other hand, the backward process is complicated and hard to be performed. Despite its ease of simulation, the forward process is a physical process and does not always need to be simulated. In contrast, despite the difficulty, the backward process should be numerically performed for accurate and quantitative OCT measurement.

1.1 Fundamental Idea and objectives of the research

Our fundamental idea is to use a deep convolutional neural network (DCNN) to solve the complicated backward process. In recent years, deep learning[18, 19] has been demonstrated to be a powerful tool in the field of computer vision. Its application in OCT, such as in image segmentation[20, 21, 22, 23], classification[24, 25], and denoising[26, 27] has been successful. The DCNN is one of the most established realizations of deep learning, which automatically learns a hierarchy of increasingly complex features related to the training data sets[28, 29, 30]. The DCNN is a highly nonlinear method and can therefore potentially solve the backward process.

In our approach, the DCNN takes a local (on the order of tens of micrometers) speckle pattern of an OCT image as an input and outputs fundamental parameters, including the

scatterer density and optical resolution. Here the scatterer density denotes the number of scatterers per unit volume. However, the DCNN should be trained using a huge training data set, and it is not realistic to acquire such a huge data set in experiments. We here solve this issue to perform simple numerical simulations of the forward process. By employing a simple model of the OCT imaging, a huge number of local speckle patterns are created for several predefined resolutions and scatterer densities; i.e., the fundamental parameters. These sets of parameters and the generated speckle patterns are used to train the DCNN. Our strategy is therefore summarized as a backward process (i.e., estimation of parameters from a local speckle pattern) performed by the DCNN and the training of the DCNN using a fully numerically generated data set that is generated by simulating the forward process. These estimators are validated by numerically generated OCT images, experimentally obtained scattering phantom images, and *in vitro* tumor spheroid images.

1.2 Organization of the Thesis

The thesis is organized as follows. Chapter two studies theory of the optical coherence tomography and generation OCT technology. Also, the theory of Deep Convolutional Neural Networks (DCNN). Chapter three includes the details of the OCT speckle pattern generator and the DCNN-based estimators. In addition, the details of the validation method using numerical validation, scattering phantom (Intralipid), biological tissue samples were also described. The theory proposed in the chapter is the basement of the DCNN estimator. Chapter four shows the outcome of the DCNN estimators and discussion. Chapter five concludes the thesis and remarks on directions for future research.

Chapter 2
Theory

2.1 Optical coherence tomography

Optical coherence tomography (OCT) [31] is a biomedical imaging modality which can non-invasively obtain cross-sectional and three-dimensional images. Figure 2.1 shows basic configuration of OCT which is based on Michelson interferometer. The light from light source is divided into a sample and reference arm. The sample beam backscattered by sample and the reference beam reflected by the reference mirror are recoupled at beam splitter, and then detected by photo detector.

The OCT imaging is done by measuring the interference signal between reference and sample beam. The axial OCT measurement is done by estimating the signal intensity and the depth where the sample beam are backscattered. The cross-sectional image is obtained by scanning the sample beam. The one-directional axial scan, the two-dimensional cross-sectional scan, and three-dimensional volumetric scan are called as A-scan, B-scan, and C-scan respectively.

2.2 OCT in ophthalmology

OCT is well-established biomedical imaging modality, and it is useful in broad fields such as ophthalmology, cardiology[32, 33, 34, 35], dentistry[36, 37, 38], dermatology[39, 40, 41], and gastroenterology[42, 43, 44]. Among the fields, ophthalmology is most suited field for OCT imaging, and have been used for diagnosis and clinical study. Because the eye is only organ of optical instrument, and hence it is perfect for investigation by optical modalities.

By using OCT, ophthalmologist can see retinal layer structure by cross-sectional imaging, and can evaluate disorders. For macular disease, OCT easily visualize lesions in the macular. Hence, OCT is helpful to diagnose macular disease such as macular hole, macular edema, and pigment epitherial detachment. OCT is also helpful to diagnose optic nerve disorders such as glaucoma. Advancement of glaucoma is evaluated by estimating nerve fiber layer thickness.

In the first demonstration of OCT, Huang *et al.*. measured *ex vivo* human retina. And only two years after the first demonstration, *in vivo* measurement of retina was demonstrated by two groups Swanson *et al.* [45] including MIT group and the Medical University of Vienna, Fercher *et al.*.[46]. In 1996, Humphrey Zeiss released first commercial OCT unit for ophthalmology. Although slow clinical adoption in early few years, OCT become an important clinical tool by technological advance of faster scan speed and increasing image quality.

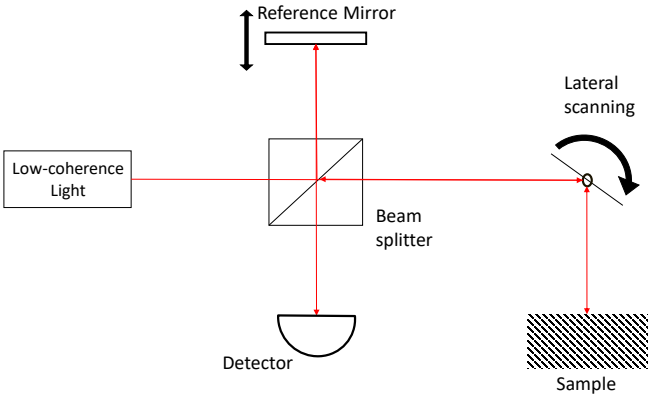

Figure 2.1 Schematic diagram of optical coherence tomography based on low-coherence interferometry

2.3 Technological advance of OCT

First generation OCT technology, so-called time domain OCT (TD-OCT) has a limitation of measurement speed. Because its axial scan is done by mechanically changing optical path length of reference arm. Second generation OCT dramatically improved the measurement speed by avoiding this mechanical scan. This OCT technology exploits Fourier domain detection, and called as Fourier domain OCT (FD-OCT).

TD-OCT uses a low-coherence light source and axial scanning reference arm. Hence, the detector detects time domain signal. In contrast, FD-OCT detects Fourier domain signal by measuring the interference spectrum. This concept was proposed in 1995 [47]. And several research groups independently demonstrated that FD-OCT has not only faster measurement speed but also powerful sensitivity advantage over TD-OCT [48, 49, 50].

FD-OCT has two subtypes of Fourier domain detection. One subtype, known as spectral domain OCT (SD-OCT), uses broad-bandwitdth light source and measures the interference spectrum by using a spectrometer and a high speed line scan camera[47, 51]. The second approach, known as swept source OCT (SS-OCT), uses a narrow-bandwidth, frequency-swept light source, and measure the interference signal as a function of time[52, 53].

FD-OCT firstly attracted the attention by its fast measurement speed. Soon it was recognized that it has another advantage of higher sensitivity than TD-OCT[48]. In TD-OCT, interference signal is caused only when the optical path length difference between reference and probe beam is shorter than coherence length. Therefore, the light which is longer than coherence length does not contribute to OCT image. On the other hand, FD-OCT is considered to be a bundle of monochromatic interferometers. For example, in SD-OCT, the output signals of each wavelength channel can be considered to be monochromatic interference between the reference and probe beams. In this interference scheme, almost all

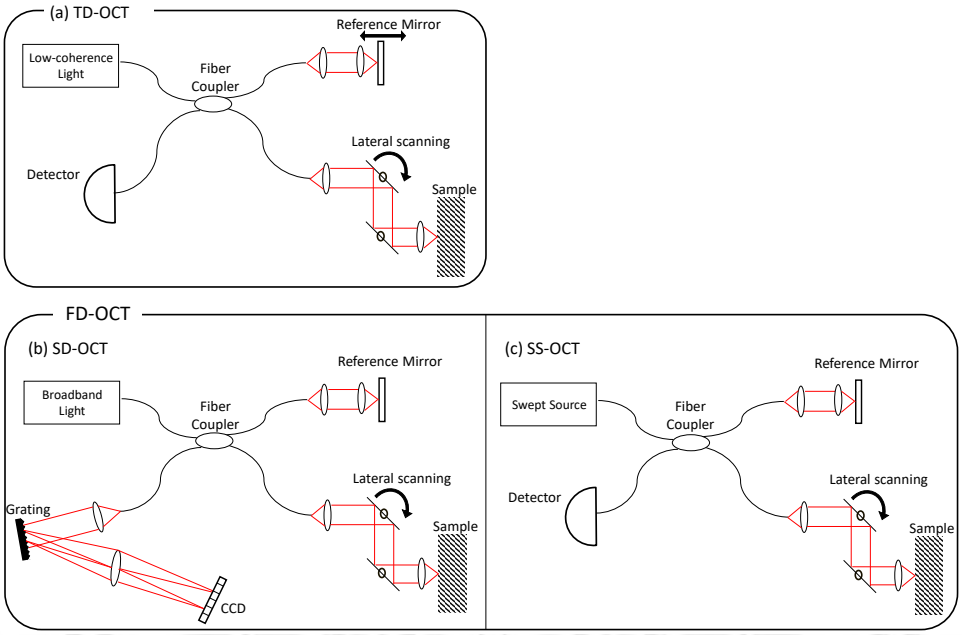

Figure 2.2 Schematic diagrams of Time- and Fourier domain OCT systems. (a) TD-OCT, (b) SD-OCT, (c) SS-OCT

properties of probe beam contribute to generating interference signal, and high-sensitivity OCT image can be achieved.

Fig. 2.2 shows schematic diagrams of three fiber-based OCT systems including (a) TD-OCT, (b) SD-OCT, and (c) SS-OCT. As shown in Fig. 2.2 (a) and (b), TD- and SD-OCT system have same Michelson interferometer part, and the difference is only light source and signal detection part. In SD-OCT, the output from broad-bandwidth light source is split into two beams by fiber coupler. The sample beam is directed onto the sample and is backscattered from internal structures of sample. The reference beam is reflected by fixed reference mirror. The signal and reference beam have a relative different path length, which is related to the depth of the structure in the tissue. And the interference between sample and reference beams is detected by using spectrometer. The relative optical path length difference can be measured by rescaling the spectrometer output from wavelength to frequency. Hence, by Fourier transforming the interference signal, it results in an axial scan measurement.

SS-OCT shown in Fig. 2.2 (c), uses a narrow bandwidth light source, which is frequency swept in time. The output from a frequency swept light source is divided into a sample and reference beam. In the sample arm, the beam is backscattered from internal structures of tissues at different depths. The reference beam is reflected from a fixed reference mirror. The difference of relative optical path length between two arms can be measured by digitizing the photodetector signal over a single frequency sweep of the light source, and Fourier transforming this beat frequency signal. This results in an axial scan measurement.

2.4 Deep Convolutional Neural Networks

Machine learning is a study field of artificial intelligence (AI) that enables systems to automatically learn and improve from experience without or with little explicit human interference. It focuses on the development of computer programs that can acquire data and build models in order to make better decisions according to prior observations or data records.

According to the adopted learning way, machine learning methods are usually categorized as being either supervised or unsupervised. In supervised learning, a model at hand is learned on a certain data along with its respective labels. Thus, once a model is learned on known data, it can be further fed with another set of data whose labels are unknown. In unsupervised learning, however, prior labels are inaccessible or accessible but unimportant for the application being addressed. This latter, thus, consists in studying how systems can infer functions to define hidden structures from unlabeled data. Semi-supervised learning is another direction whose aim is to exploit a small-sized label data and a large-sized unlabeled data.

A close look at the recent literature would tell that a big focus is being oriented towards deep learning. By contrast to traditional Neural Networks, various layers of neurons in deep learning perform a hierarchical learning of the data representation via non-linear transformations. In other words, the data is passed cumulatively across a long chain of layers (thus, the description deep), where each layer can be fully or partially connected to the preceding one. Although deep architectures have long existed, the term "deep learning" was first introduced in 2006 by Hinton *et al.* [54], where they showed that a multilayer feedforward neural network can be more efficient by applying pretraining of one layer at a time and considering each layer as an unsupervised Restricted Boltzmann Machine, by using supervised back propagation for finetuning.

One year later, Bengio *et al.* [55] developed the Stacked Auto-Encoder, which is a deep architecture based on the concatenation of many Auto-Encoders. Each Auto-Encoder has three layers, one visible layer (input), one hidden layer and one reconstruction layer with similar size as the input. Another famous deep architecture is Deep Convolutional Neural Network (DCNN) [18, 24]. DCNNs are generally composed of many layers, where each layer has two parts, one for convolution (filtering) and one for pooling (subsampling). The chain of convolutional/pooling layers is normally concluded by a regression layer (e.g., logistic regression) in order to discern the class label of the image/object presented as input to the network. DCNNs are shaped in a 2D structure, which offers the advantage of directly processing the raw images. This can be achieved with local connections and tied weights followed by subsampling. Yet, it is evident that deep models in general, and DCNNs in particular, undergo a heavy processing, which demands highly powerful computation machines. Figure 2.3, Figure 2.4 and Figure 2.5 show examples of architectures of a RBM, an AE and a deep CNN.

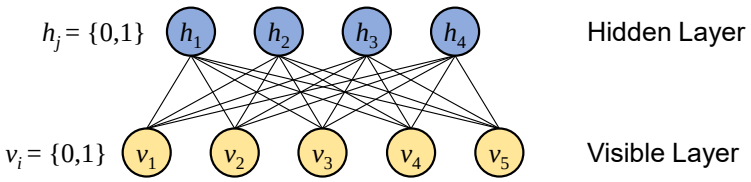

Figure 2.3 The network structure of Restricted Boltzmann Machine.

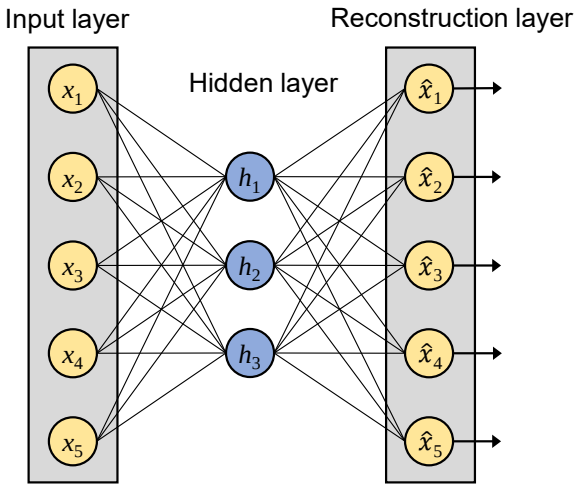

Figure 2.4 The network structure of an auto-encoder.

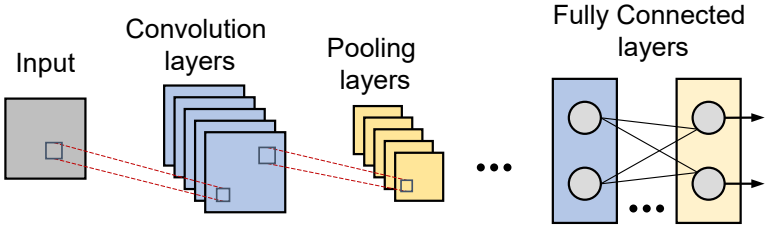

Figure 2.5 A simple deep convolutional neural network model architecture.

Chapter 3
Method

This chapter present deep convolutional neural network (DCNN)-based estimators of the tissue scatterer density, lateral and axial resolutions, signal-to-noise ratio (SNR), and effective number of scatterers (ENS, the number of scatterers within a resolution volume). The estimators analyze the speckle pattern of an optical coherence tomography (OCT) image in estimating these parameters. The details are as follows.

3.1 Three-dimensional speckle pattern generator

Generation small volumetric OCT speckle patterns in a simulation based on a simple Fourier imaging model. A three-dimensional (3D) scatterer distribution map, $S(x, y, z)$, is first generated stochastically to generate the speckle pattern. Here x and y are lateral positions and z is the depth position. The 3D scatterer distribution map is a complex 3D numerical array with 16 $\times$ 16 $\times$ 16 pixels, where the pixels with a scatterer (i.e., scatterer pixels) have an amplitude of unity and a random phase whereas the pixels without scatterer have zero values. The scatterer pixels are randomly selected such that the expectation of the scatterer density of the distribution map is a particular set value. The random phases of the scatterer pixels represent the randomly distributed sub-wavelength position of the scatterers.

This 3D scatterer distribution map is then numerically convolved with a 3D complex point spread function (PSF), PSF(x, y, z), to yield a simulated complex OCT signal $G(x, y, z)$ as

$$G(x, y, z) \equiv S(x, y, z) * \text{PSF}(x, y, z), \tag{3.1}$$

where $G(x, y, z)$ is the 3D speckle pattern and $*$ indicates the 3D convolution. The PSF is numerically generated as a 3D Gaussian function whose axial and lateral widths (i.e., resolutions) are randomly selected. Here, the axial and lateral resolutions are respectively defined as the full-width-half-maximum (FWHM) and $1/e^2$-width of the squared amplitude of the PSF. It is noted that the lateral resolutions along x and y are selected to be identical. The axial and lateral resolutions are ones of our estimation target. Additionally, the magnitude of the PSF is randomly selected to simulate the uncontrolled probe beam power and unknown scattering intensity. After generating the local speckle patterns, we add complex Gaussian noise to achieve a randomly but specifically selected signal-to-noise ratio (SNR) then taking the squared intensity of the 3D OCT speckle pattern.

The generated 3D speckle pattern covers a 31.2-μm (x) $\times$ 31.2-μm (y) $\times$ 115.8-μm (z) volume with 16 $\times$ 16 $\times$ 16 pixels. The pixel separations of the generated speckle pattern are selected to be identical to those in our experiment described in Section 3.4. The inputs for the training of the DCNN-based estimator described in the next section are 2D cross-

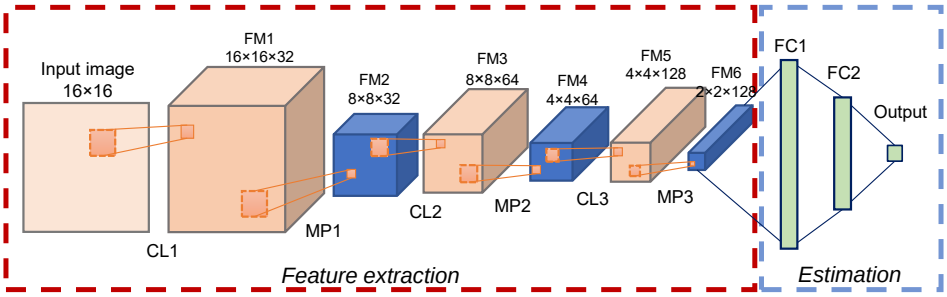

Figure 3.1 Architecture of the network used for parameter estimation. CL; convolution layer, FM; feature map, MP; max-pooling layer, and FC; fully connected layer. The numbers above the boxes are the sizes of the boxes as pixel × pixel × filters.

sectional OCT images, which are the x-z cross-sections of the 3D numerically generated speckle pattern.

3.2 DCNN-based parameter estimator

3.2.1 Speckle data set

The data set for DCNN training is generated by the 3D speckle pattern generator described in the previous section. The true parameters are randomly selected with specific ranges of 3 to 30 μm for the axial and lateral resolutions, 0 to 50 dB for SNR, and 0 to 0.0645 scatterers/μm^3 (0 to 1.775 scatterers/pixel^3) for the scatterer density. The speckle patterns are normalized by intensity before being input to the DCNN, and the PSF magnitude is thus not a significant parameter. Each datum in the data set is the combination of the speckle pattern and the set fundamental parameters.

The training data set consists of 1,280,000 2D cross-sectional speckle patterns extracted from 80,000 3D speckle patterns. The validation data set, which is used to compute the loss during the training, comprises 160,000 2D speckle patterns extracted from 10,000 3D speckle patterns.

3.2.2 Network architecture and Training

Our DCNN model architecture is shown in Fig. 3.1. The DCNN is input with the 2D cross-sectional speckle patterns, and it automatically learns the local features of the speckle pattern and estimates the underlying parameters. The whole network is subdivided into two parts, namely the feature extraction and the estimation parts.

The input to the feature extraction part is a 2D cross-sectional speckle image with a size of 16 × 16 pixels [input image in Fig. 3.1]. The input image intensity is normalized to a [0, 1] range before being input. The first convolution layer (CL1) convolves the image with 32 different filters having a kernel size of 2 × 2 to obtain a feature map (FM1; 16 × 16 pixels × 32 filters). Here, the rectified linear unit (ReLU) is used as an activation function.

A max-pooling layer (MP1) with a stride of 2 is applied after the convolution, which fuses nearby spatial information reduce the size of the feature map. The second convolution layer (CL2) produces the third feature map (FM3; 8 × 8 pixels × 64 filters) using 2 × 2-pixel kernels and ReLU activation. After applying a max-pooling layer with a stride of two (MP2), the third convolutional layer (CL3) generates the fifth feature map (FM5; 4 × 4 pixels × 128 filters). Finally, the third max-pooling layer (MP3) makes the final feature map (FM6; 2 × 2 pixels × 128 filters), and feeds the subsequent estimation part.

The estimation part consists of two fully connected layers of FC1 and FC2 which consist of 512 and 256 neurons, respectively. The final output layer consists of a single neuron and its output is an estimated fundamental parameter.

We train our neural network models to minimize the mean squared error (MSE) between ground-truth parameters and network outputs. The network is trained using an Adam optimizer[56] with a learning rate of 10^{-4}. Five independent networks with the same network architecture are trained for five fundamental parameters, namely the scatterer density, the lateral and axial resolutions, SNR, and effective number of scatterers (ENS). The ENS is the number of scatterers within a 3D resolution volume. It is noteworthy that the SNR is randomized and the signal strength is normalize, and hence, a DCNN might not use this information to estimate the scatterer density and ENS.

The models are constructed in Python 3.7 with Keras 2.3.1 based on the TensorFlow back end. The training of each network with a graphical processing unit (GPU; Nvidia GTX1080) takes about 5-6 min for each epoch. The training is terminated if the loss has not decreased for 10 continuous epochs, and the weights with the minimum loss are selected for the estimator. The minimum loss is obtained at the 30th, 28th, 27th, 15th and 28th epochs for the scatterer density, lateral and axial resolutions, SNR, and ENS, respectively.

3.3 Validation methods

The DCNN-based estimators are validated using numerically generated OCT signals, experimentally measured OCT images of the scattering phantom and an *in vitro* spheroid sample. The details are as following.

3.3.1 Numerical validation

We evaluated the estimation performances of the DCNN-based estimators using 100 numerically generated OCT speckle patterns. The speckle patterns are generated with the same method used to generate the training data set, but they are not included in the training or validation data set. Here, the evaluation performances for the scatterer density, ENS, the lateral and axial resolutions, and SNR are evaluated. The true values are known for this evaluation, and we can thus obtain the estimation accuracies.

3.3.2 Validation by scattering phantom measurement

The DCNN-based estimators were validated experimentally by measuring scattering phantoms; the Intralipid emulsion. In the field of biomedical optics, 20% Intralipid emulsion (IL-20; I141, Sigma-Aldrich) is frequently used as an optical phantom to mimic the optical properties of tissue[57]. Six different dilutions were made by mixing the IL-20 with purified water to obtain concentrations of 1%, 2%, 4%, 6%, 8%, and 10%. Each dilution was then placed in a Petri dish. Black mending tape was attached at the bottom of the Petri dish to avoid strong specular reflection from the glass surface. Three samples were made for each concentration, i.e., 18 samples were made in total.

The scattering of light by Intralipid emulsion is due to the particles of soybean oil and egg lecithin, and the scattering volume concentration σ of IL-20 is known to be 22.7%(v/v) [58, 59, 60]. Hence, the scattering volume concentrations of the 1%, 2%, 4%, 6%, 8%, and 10% dilutions are 0.227 0.454, 0.908, 1.362, 1.816, and 2.27%(v/v), respectively.

3.3.3 Human breast cancer spheroid

The scatterer density estimator was also applied to an *in vitro* sample. The sample was a human breast adenocarcinoma spheroid made from MCF7 cell line. The scatterers in the cell are cell nuclei and cell organelles, and we thus anticipated that the scatterer density was strongly related to tissue functions.

After 15-day cultivation, spheroids with a size of a few hundred micrometers had formed. The spheroid was extracted from the culturing environment and placed in a room-temperature culture medium without CO_2 supply. The cell might have been gradually dying because of a lack of nutrients. We performed OCT measurement every 2 hours up to 28 hours. Note that this experiment was originally performed for the study described in Ref. [61], and the same data set was used in the present study.

3.4 OCT setup and measurement protocol

Swept-source OCT with a 1.310 μm wavelength probe beam and a measurement speed of 50,000 A-lines/s was conducted in the experiments[62]. Although the system was polarization-sensitive, we did not use its polarization functionality. The OCT image used in this study is the coherence composition of multiple polarization channels (Section 2.3.1 of Ref. [62] and Section 3.8 of Ref. [63]), which is almost equivalent to a standard OCT image.

Two objectives were used in this study. One has an effective focal length of 18 mm (LSM02, Thorlabs Inc., NJ). The beam diameter incident on the objective is 3.49 mm, and the effective numerical aperture (NA) was thus 0.097. This resulted in a diffraction-limit lateral resolution (spot size)[64] of 8.6 μm, whereas the lateral resolution numerically simulated by OpticStudio (Zemax) is 8.9 μm. We refer to this objective as a high-NA objective. The other objective, a low-NA objective (LSM03, Thorlabs Inc., NJ) had an effective focal length of 36 mm. The effective NA of 0.048 results in a diffraction-limit lateral resolution is 17.2

μm, whereas the numerically simulated resolution is 18.1 μm.

Each B-scan comprises 512 A-lines covering a lateral scanning range of 1 mm, and the lateral pixel separation is 1.95 μm. The axial resolution of our system is 14.1 μm and the axial pixel separation is 7.24 μm in tissue. These axial and lateral pixel separations are identical to those of the numerically generated speckle patterns (Section 3.1).

The measurements were performed for several values of probe beam attenuation, namely 0 dB, -5.4 dB, and -11.76 dB (for round trip). The probe power on the sample was 12 mW with 0-dB attenuation.

Chapter 4
Results and Discussion

4.1 Results

4.1.1 Numerical validation

All DCNN-based parameter estimators show high consistency between the set and estimated parameters as shown in Fig. 4.1. Figure 4.1(a)-(e) are for the scatterer density, ENS, lateral and axial resolutions, and SNR, respectively. The horizontal axes represent the set parameters whereas the vertical axes show the estimates.

The root mean square errors (RMSEs) of the estimation are 0.113 scatterrs/μm^3 for the scatterer density, 3.06 scatterers for the ENS, 1.78 μm for the lateral, 1.88 μm for the axial resolutions, and 1.82 dB for the SNR. These RMSEs correspond to 0.23%, 6.15%, 3.58%, 3.79%, and 3.65% of the estimation ranges, respectively. Here, the estimation ranges are the ranges of each parameter in the speckle generation. R^2 values of a model "estimate = true value" are 0.955 for the scatterer density, 0.985 for the ENS, 0.947 for the lateral resolution, 0.951 for the axial resolution, and 0.985 for the SNR. The estimators therefore give the reasonable estimates of the parameters.

4.1.2 Scattering phantom

Scatterer density estimation

Figure 4.2 shows the example OCT B-scans of the scattering phantom with the concentration of 0.227%(v/v), where Figs. 4.2(a) and 4.2(b) are obtained with the high- and low-NA objectives, respectively. We process these images using the scatterer density estimator having a sliding window of 16 $\times$ 16 pixels and computed the average scatterer density within the Intralipid region. Figure 4.3 shows the average scatterer density at each scatterer concentrations for each of three probe-beam attenuations. Figures 4.3(a) and 4.3(b) show results for the high-NA and low-NA objectives, respectively. Three phantoms were measured for each concentration, and the error bars in the plots represent the standard deviations among the three measurements of the three samples.

It is found that the results are consistent for the high- and low-NA objectives. It is also noteworthy that the estimations are not affected by the probe beam attenuation, i.e., the probe power. This suggests that the estimator does not estimate the scatterer density from the OCT signal strength.

The estimated scatterer densities have a linear relationship with the concentration. The average slopes of the three measurements (three phantoms) are 0.5622 (for -0 dB attenuation), 0.5436 (-5.4 dB), and 0.5577 (-11.76 dB) μm^{-3}/%(v/v) for the high-NA objective, and 0.5560 (-0 dB), 0.5587 (-5.4 dB), and 0.5415 (-11.76 dB) μm^{-3}/%(v/v) for the low-NA

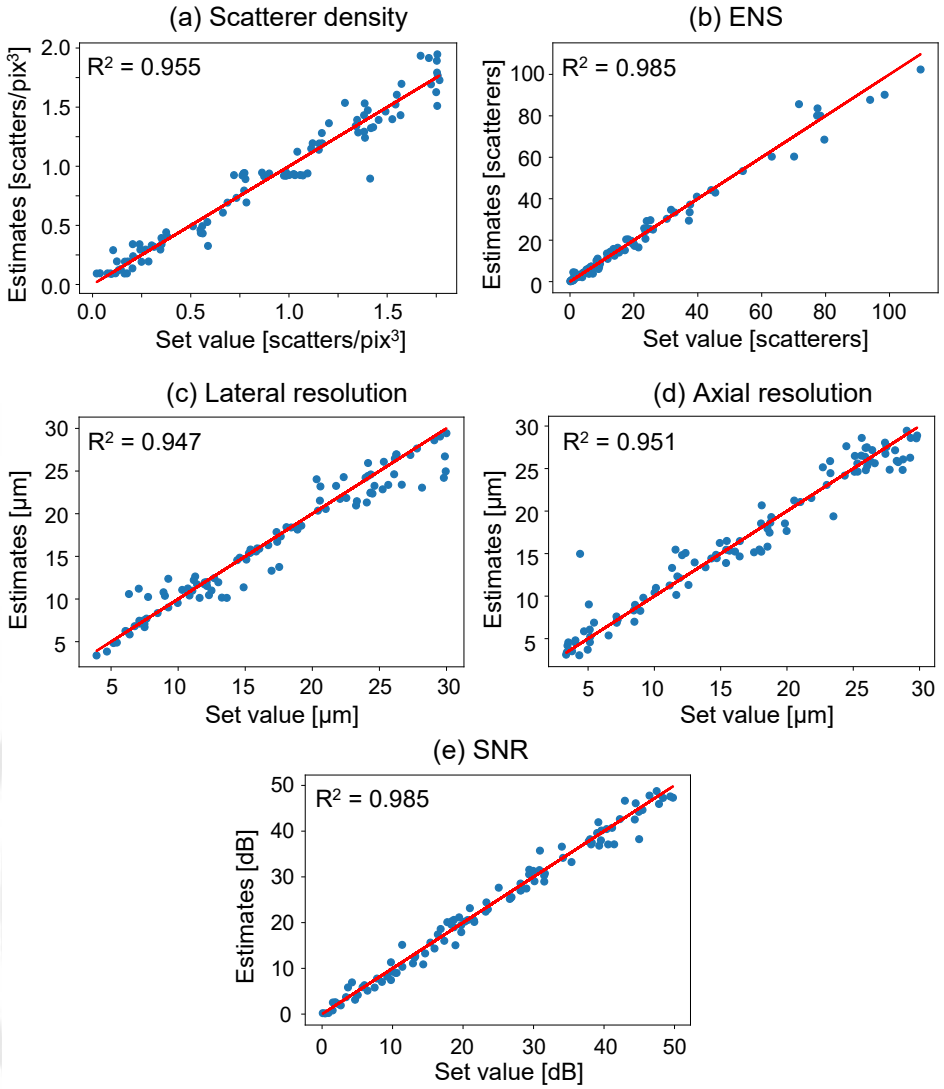

Figure 4.1 Numerical validation of the parameter estimations of scatterer density (a), ENS (b), lateral resolution (c), axial resolution (d), and SNR (e). The horizontal and vertical axes give the set (true) values and the estimates, respectively. The red lines show the perfect estimation.

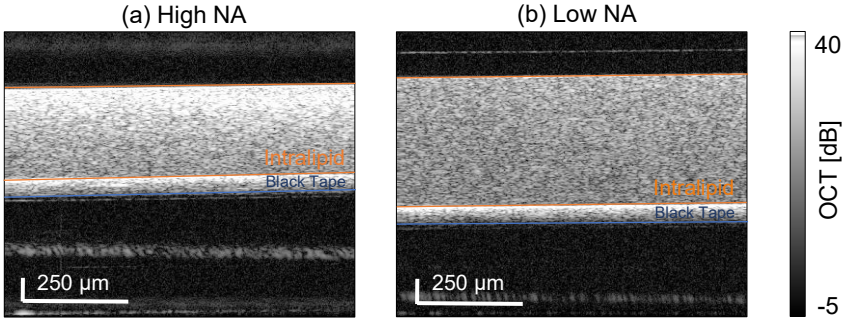

Figure 4.2 Example OCT images of a scattering phantom with a concentration of 0.227% (v/v). (a) and (b) are images obtained with the high- and low-NA objectives, respectively.

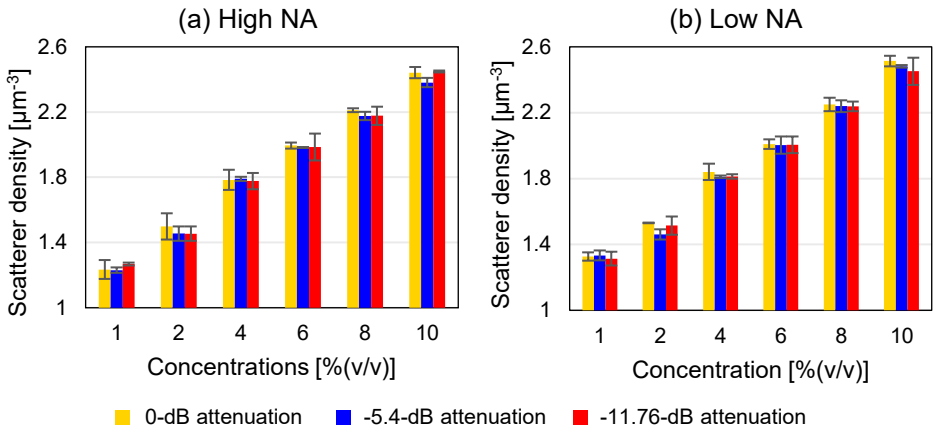

Figure 4.3 Scatterer density estimation of the Intralipid phantoms with several volume concentrations. (a) and (b) are the results obtained with the high- and low-NA objectives, respectively, and the color represent different attenuation of the probe beam. The error bars depict the standard deviations for three measurements of three phantoms.

objective.

We can compute the scatterer size from these slopes as discussed in detail in Section 4.2.1. The intercepts of plots are found not to be zero, although the ideal intercept is zero. The intercepts are 1.23 (for -0 dB attenuation), 1.20 (-5.4 dB), and 1.20 (-11.76 dB) μm^{-3} for the high-NA objective, and 1.26 (-0 dB), 1.23 (-5.4 dB), and 1.25 (-11.76 dB) μm^{-3} for the low-NA objective. This issue is discussed in Section 4.2.4.

To evaluate the depth dependency of the scatterer density estimation, the estimated scatterer densities are averaged along the lateral direction (red lines in Fig. 4.4). Here, the data correspond to those in Fig. 4.2 and the concentration is 0.227%(v/v). The blue lines indicate the average OCT intensity and the region between the dashed lines is the region of the Intralipid. The strong OCT signals at just beneath the Intralipid region (dash line) are from black mending tape placed at the bottom of the Petri dish.

It is found that the estimated scatter densities are almost constant along the depth, and they are consistent among the NAs. It is also found that the estimated scatterer densities are independent of the average OCT intensity. The mean scatterer densities in the Intralipid region are 1.37 scatterers/μm^3 and 1.35 scatterers/μm^3 for the high- and low-NA objectives, respectively, i.e., the difference is only 1.5%.

Attenuation coefficients or the signal attenuation rate along the depth are frequently used to evaluate the scattering property of a sample. The attenuation rates of these data are computed through linear regression of the OCT intensity as -24.8 dB/mm (for the high-NA) and -6.8 dB/mm (for the low-NA). This relatively large inconsistency (8%) is accounted in part by the different focus positions and the different depth-of-focuses of the two measurements.

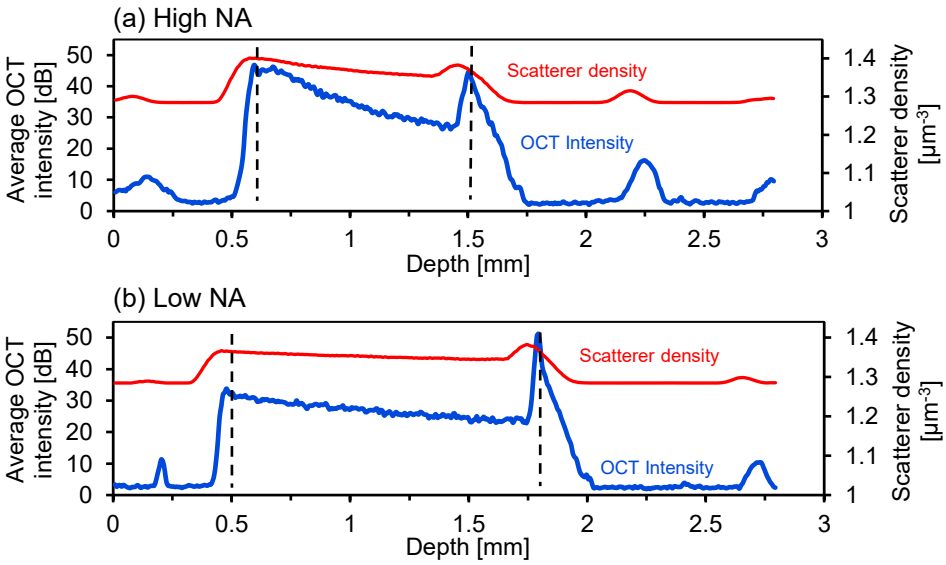

Figure 4.4 Depth profiles (blue lines) and the estimated scatterer density (red lines) of the phantom shown in Fig. 4.2.

Resolution estimation

Figure 4.5 shows the resolution estimation results of the scattering phantom. The data correspond to those of Fig. 4.2. The blue regions indicate the region of Intralipid.

The average estimates of the lateral resolution over the Intralipid region were 9.6 μm and 18.8 μm for the high- and low-NA objectives, respectively [Fig. 4.5(a) and 4.5(b)]. These estimates are close to the numerically simulated in-focus lateral resolutions of 8.9 μm (high NA) and 18.1 μm (low NA). It is also noteworthy that the lateral resolution of the high-NA objective shows significant depth dependency. This can be accounted for by the short depth of focus (88.7 μm in theory and 95.0 μm by Zemax simulation, in air), whereas the depth of focus of the low-NA objective is relatively long (355.0 μm in theory and 392.8 μm by Zemax simulation, in air).

The average axial resolution estimates are 14.1 μm and 13.9 μm, respectively for the high- and low-NA objectives [Fig. 4.5(c) and 4.5(d)]. These estimates are close to the true depth resolution of 14.1 μm.

4.1.3 Time-course evaluation of a tumor spheroid

The scatterer density estimator is applied to the time-lapse images of an *in vitro* human breast cancer spheroid measured up to 28 hours after the extraction from the cultivation environment (Fig. 4.6). The first and second rows [Fig. 4.6(a) and (b)] show the conventional OCT and scatterer density image, respectively. It is noted that the estimation window is relatively large, i.e., 31.2 μm (lateral) $\times$ 115.8 μm (depth), in comparison with the spheroid size (around 400 μm in diameter), and the estimates at the spheroid periphery are thus not exactly reliable. Figures 4.6(c) and 4.6(d) show the tissue dynamics images [61] for reference.

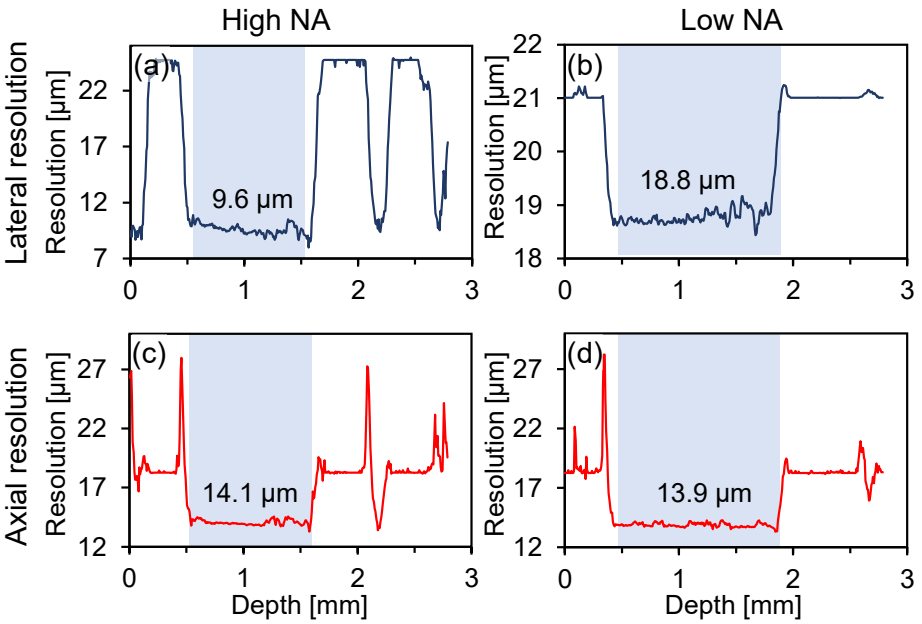

Figure 4.5 Resolution estimates of scattering phantoms (0.227%(v/v)). The first and second columns are for the high- and low-NA objectives, and the first and second rows show the lateral and axial resolutions, respectively. The blue background indicates the Intralipid region.

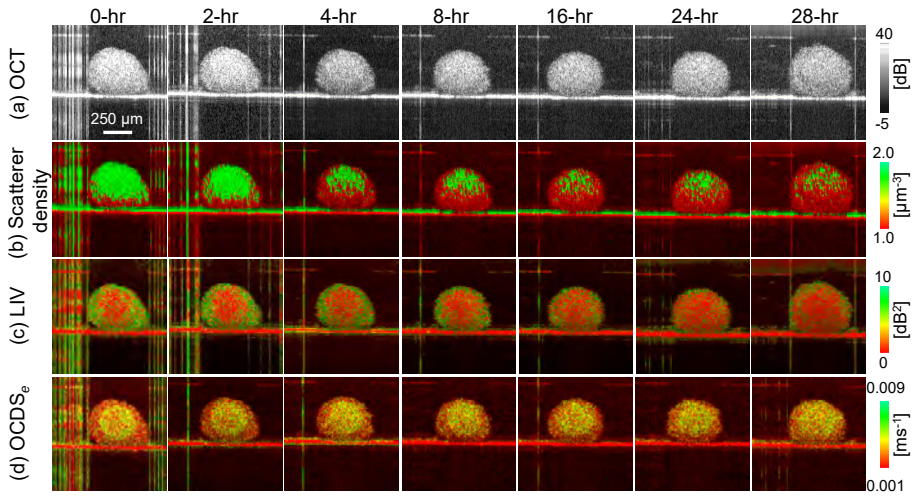

Figure 4.6 Time-lapse images of a human breast adenocarcinoma spheroid (MCF7): (a) conventional OCT, (b) scatterer density images obtained using the DCNN-based scatterer density estimator, (c) magnitude of the signal fluctuation (LIV), (d) decorrelation speed of the OCT signal (OCDS$_e$).

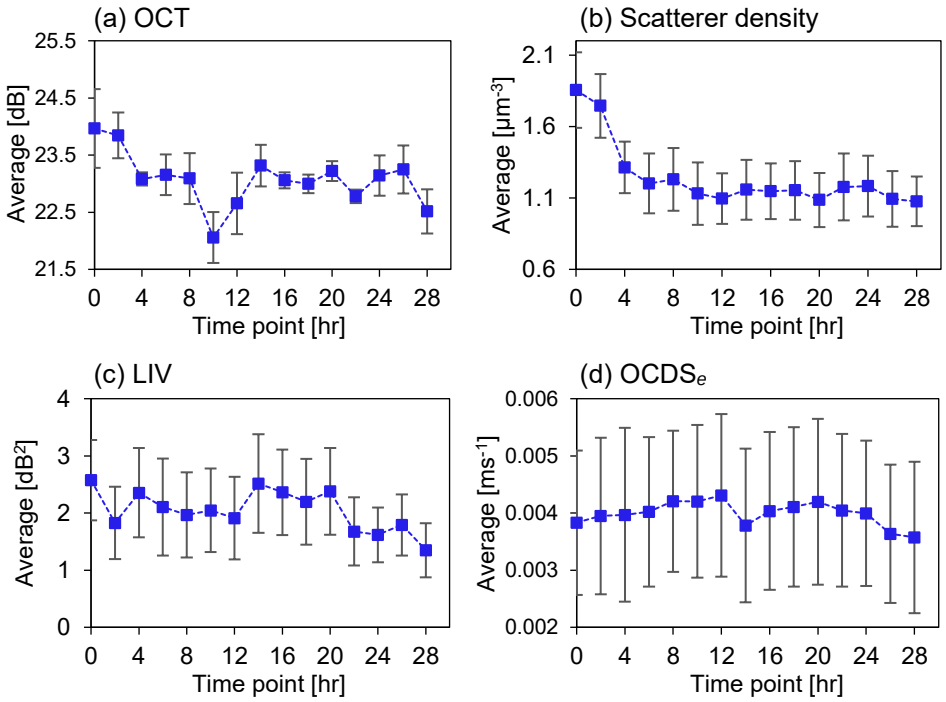

Figure 4.7 Time courses of the average OCT intensity (a), scatterer density (b), LIV (c), and $OCDS_e$ (d) in the central region of the spheroid (lateral 117 μm × axial 144.8 μm).

Figure 4.6(c) presents the "logarithmic intensity variance" (LIV), which is primarily sensitive to the magnitude of the signal intensity fluctuation, i.e., it is sensitive to the magnitude of the intracellular motility. Figure 4.6(d) presents the "OCT correlation decay speed at early delay time" ($OCDS_e$), which reflects the speed of the signal decorrelation. $OCDS_e$ has a large value if there is a rapid motion in the cell. These images are reprinted from our previous publication [61].

Figure 4.7 shows the time courses of the average OCT intensity (a), scatterer density (b), LIV (c), and $OCDS_e$ (d) in regions of interest (ROI) around the center of the spheroid. The size of the ROI is lateral 117 μm × axial 144.8 μm (60 × 20 pixels). The bars in the plots indicate the standard deviations.

The conventional OCT intensity [Fig. 4.6(a)] does not change appreciably over 28 hours and the average OCT signal intensity [Fig. 4.7] fluctuates with time and does not have a clear tendency. Meanwhile, the region with high scatterer density (green) rapidly becomes small over the first 8 hours [Fig. 4.6(b)]. Additionally, the average scatterer density [Fig. 4.7(b)] rapidly reduces over the first 8 hours. The low LIV region (red) and high $OCDS_e$ region (yellow to green) became large with time [Fig. 4.6(c) and (d)]. Additionally, the average LIV gradually reduces with time [Fig. 4.7(c)]], but this reduction is slower than that of the scatterer density [Fig. 4.7(b)].

The low LIV and high $OCDS_e$ are thought to indicate cell necrosis[65, 61]. The main scatterers in the cell are cell nuclei and cell organelles, and the rapid reduction of the scatterer density therefore suggests the destruction of nuclei and organelles during necrosis.

4.2 Discussion

4.2.1 Scatterer diameter of the Intralipid

The scatterers of the Intralipid are the particles of soybean oil and egg lecithin [58, 59, 60]. Assuming the scatterer particles are spherical, the scatterer density (the number of scatterers per unit volume) of the Intralipid dilution can be computed as

$$\text{Scatterer density} = \frac{\sigma}{4\pi/3\,(d/2)^3}, \tag{4.1}$$

where σ is volume concentration of the scattering medium and d is the diameter of the scatterer particle. Using this equation, the diameter of scatterer particle can be computed from the slope of the relation between the scatterer density and σ as

$$d = \sqrt[3]{6/(\pi\,\text{slope})}. \tag{4.2}$$

In our Intralipid phantom measurements (Section 4.1.2), the slope of the relation between the scatterer density and σ is found to be 0.5533 $\pm$ 0.0086 μm^{-3}/%(v/v), or equivalently 55.33 $\pm$ 0.86 μm^{-3}/(v/v ratio) (mean $\pm$ standard deviation over three attenuations and two NAs). The diameter of the scatterer particle is thus estimated to be 325.6 nm. Previously reported scatterer particle diameters of Intralipid vary in the literature; e.g., 25 to 473.9 nm [60], 50 to 400 nm with 225.7-nm mean diameter [58], and 360 nm [59]. The diameter estimated in the present study is well within the range of reported diameters.

4.2.2 Benefits of numerically synthesized training data set

The present DCNN based estimators were trained by a numerically synthesized data set. The numerical generation of the training data set has several advantages against experimentally collecting a training data set.

At first, a massive amount of training data can be obtained with negligible cost. In the present study, 1,280,000 2D speckle patterns extracted from 80,000 3D synthesized OCT volumes were used for training (Section **??**).

Second, the training data can have high diversity of the ground-truth fundamental parameter values. For instance, all the 80,000 synthesized OCT volumes were generated with different fundamental parameters in the present study. It might make the DCNN-based estimator robust. If we achieve the same diversity of the ground-truth parameters with an experimental data set, 80,000 accurately fabricated phantoms are required, and it is not realistic.

Third, some of the fundamental parameters are not really controllable in the experiment. For example, the lateral and axial resolutions are defined by the OCT device. And using massive amounts of OCT devices to prepare the training data set with a variety of resolutions is not realistic.

Finally, it is noteworthy that some of the fundamental parameters are hard to be accurately controlled in the experiment. As pointed out by Kübler *et al.*, the same recipe of the

phantom does not always give the same scattering property[**?**]. In addition, the resolutions are affected by the aberrations, dispersion, wavelength-dependent absorption, and so on. And hence, it is hard to control or know the accurate resolutions in the experiment.

4.2.3 Rationality of the estimation of the signal-strength-independent scatterer density

The speckle patterns and OCT images are normalized by intensity before being input to the DCNN-based estimator, and the estimator therefore cannot use the overall signal strength to estimate the scatterer density. This is consistent with the results shown in Fig. 4.3, where the scatterer density estimates are not sensitive to the probe beam attenuation.

This signal-strength-independent estimation process is reasonable for the following reasons. First, Hillman *et al.* showed that the contrast of a local speckle pattern has a unique and monotonical relationship with the ENS, i.e., the number of scatterers per coherence volume that is an alias of the 3D resolution[2]. This suggests that the ENS can be estimated from the speckle contrast in principle.

In addition, if we know the size of the coherence volume, we can estimate the scatterer density (i.e., the number of scatterers per unit volume) from the ENS. The size of the coherence volume can be estimated if the axial and lateral resolutions are known. Kurokawa *et al.* showed that these resolutions can be estimated through the spatial correlation analysis of a local speckle pattern [3].

That is to say, we can estimate both the ENS and the coherence volume size from the local speckle pattern. Hence, estimation of the scatterer density without information of the overall signal strength is possible in principle.

In the present study, the DCNN-based estimators successfully estimate the ENS and the resolutions (Sections 4.1.2 and 4.1.2), which further supports the rationality of the estimation.

The forgoing discussion gives the idea that the scatterer density can be computed by combining the speckle contrast analysis of Hillman and the correlation analysis of Kurokawa. However, it is difficult to accurately compute the speckle contrast and correlation because of noise in the speckle pattern. One strength of our DCNN-based estimator is that it can be trained to be robust against noise by adding random noise to the speckle patterns of the training data set.

4.2.4 Limitation of the current estimators

The current estimation framework has limitations. First, the speckle generator does not consider the size of the scatterers. The speckle generator uses a 3D numerical field in which the voxel size is 1.95 μm $\times$ 1.95 μm $\times$ 7.24 μm (lateral $\times$ lateral $\times$ depth), and a single scatterer correspond to a single voxel. This low accuracy of the scatterer representation can reduce the accuracy of the estimation.

The second limitation is that the speckle generator does not account for depth-dependent signal attenuation. That is to say, the signals in the deeper region are not affected by the scattering or absorption in the superior region. Although we expect this effect to be small as the depth of the generated speckle pattern is only 115.8 μm, the estimator accuracy could be further improved by taking this effect into account.

Third, the sensitivity roll-off, depth-dependent variation of noise floor, and confocal effect [66] were not accounted for in our speckle generator. These factors can affect the estimation accuracy as it alters the SNR within the estimation window. However, for our small estimation window whose depth size is 115.8 μm, the effects of these factors might be limited. The estimation accuracy can be further improved by accounting these factors in the speckle generation process.

Fourth, in the speckle pattern generator, the scatterers are assumed to be static. Therefore, the jiggle of the Intralipid scatters due to Brownian motion is not accounted for. In addition to the above two limitations, this discrepancy would partially explain the non-zero intercept in Fig. 4.3.

Fifth, our study only considers fully developed speckle patterns and does not account for partially developed speckles. Although this might limit the accuracy and the applicability of the estimators, we believe our current estimators are still reasonable. It is because several previous studies of OCT are based on the assumption of fully developed speckles, and they have given reasonable results [1, 67, 2].

We expect further improvement of the speckle generator will increase the accuracy of the estimators.

Chapter 5
Conclusion

In this study, We demonstrated DCNN-based estimators for the scatterer density, ENS, lateral and axial resolution, and SNR. The DCNN is trained using fully numerically generated OCT images (i.e., speckle patterns) and was therefore trained easily using an extremely large training data set comprising 1,280,000 images. Numerical validation showed the good performance of the estimators. Additionally, validation with the scattering phantoms showed the feasibility of the estimators in experiments. The scatterer density estimator was also applied to an *in vitro* tumor spheroid, and the reduction of the scatterer density during cell necrosis was visualized.

In conclusion, the DCNN-based estimators successfully extract fundamental parameters from a local speckle pattern. The scatterer density estimator can be used to quantify a cell microstructure smaller than the OCT resolution. Furthermore, the resolution estimators can be used as optimization metrics of image-based adaptive optics or computational aberration correction and also for the calibration of OCT systems, such as in highly accurate measurements of the attenuation coefficient.

In the future, we will further improve the present work by deploying the algorithm of 3-dimension convolutional to deal with the 3D speckle pattern to improve model performance. Besides, a speckle pattern will also be challenged in this method to evaluate this model algorithms' performance on this system in a qualitative way. As revealed in subsection 4.2.2 and 4.2.4, there is still room to improve it. A further discussion on this board is also the key to improving this work.

Bibliography

[1] J. M. Schmitt, S. H. Xiang, and K. M. Yung, “Speckle in optical coherence tomography,” **J. Biomed. Opt.**, vol. 4, pp. 95–105, 1999.

[2] T. R. Hillman, S. G. Adie, V. Seemann, J. J. Armstrong, S. L. Jacques, and D. D. Sampson, “Correlation of static speckle with sample properties in optical coherence tomography,” **Opt. Lett.**, vol. 31, no. 2, pp. 190–192, Jan. 2006. [Online]. Available: https://www.osapublishing.org/abstract.cfm?URI=ol-31-2-190

[3] K. Kurokawa, S. Makita, Y.-J. Hong, and Y. Yasuno, “In-plane and out-of-plane tissue micro-displacement measurement by correlation coefficients of optical coherence tomography,” **Opt. Lett.**, vol. 40, no. 9, pp. 2153–2156, May 2015. [Online]. Available: https://www.osapublishing.org/abstract.cfm?URI=ol-40-9-2153

[4] P. Wijesinghe, L. Chin, and B. F. Kennedy, “Strain tensor imaging in compression optical coherence elastography,” **IEEE J. Sel. Topics Quantum Electron.**, vol. 25, no. 1, pp. 1–12, Jan. 2019. [Online]. Available: https://ieeexplore.ieee.org/document/8470111/

[5] K. A. Vermeer, J. v. d. Schoot, H. G. Lemij, and J. F. d. Boer, “RPE-normalized RNFL attenuation coefficient maps derived from volumetric OCT imaging for glaucoma assessment,” **Invest. Ophthalmol. Visual Sci.**, vol. 53, no. 10, pp. 6102–6108, Sep. 2012. [Online]. Available: http://www.iovs.org/content/53/10/6102

[6] K. A. Vermeer, J. Mo, J. J. A. Weda, H. G. Lemij, and J. F. de Boer, “Depth-resolved model-based reconstruction of attenuation coefficients in optical coherence tomography,” **Biomed. Opt. Express**, vol. 5, no. 1, pp. 322–337, Jan. 2014. [Online]. Available: https://www.osapublishing.org/boe/abstract.cfm?uri=boe-5-1-322

[7] T. M. Cannon, B. E. Bouma, and N. Uribe-Patarroyo, “Layer-based, depth-resolved computation of attenuation coefficients and backscattering fractions in tissue using optical coherence tomography,” **Biomed. Opt. Express**, vol. 12, no. 8, pp. 5037–5056, Aug. 2021. [Online]. Available: https://www.osapublishing.org/abstract.cfm?URI=boe-12-8-5037

[8] A. C. Chan, K. Kurokawa, S. Makita, M. Miura, and Y. Yasuno, “Maximum a posteriori estimator for high-contrast image composition of optical coherence tomography,” **Opt. Lett.**, vol. 41, no. 2, pp. 321–324, Jan. 2016. [Online]. Available: https://www.osapublishing.org/abstract.cfm?URI=ol-41-2-321

Bibliography (Continue)

[9] A. C. Chan, Y.-J. Hong, S. Makita, M. Miura, and Y. Yasuno, "Noise-bias and polarization-artifact corrected optical coherence tomography by maximum a-posteriori intensity estimation," **Biomed. Opt. Express**, vol. 8, no. 4, pp. 2069–2087, Apr. 2017. [Online]. Available: https: //www.osapublishing.org/abstract.cfm?URI=boe-8-4-2069

[10] D. Kasaragod, S. Makita, S. Fukuda, S. Beheregaray, T. Oshika, and Y. Yasuno, "Bayesian maximum likelihood estimator of phase retardation for quantitative polarization-sensitive optical coherence tomography," **Opt. Express**, vol. 22, no. 13, pp. 16 472–16 492, Jun. 2014. [Online]. Available: http://www.opticsinfobase.org/oe/abstract.cfm?uri=oe-22-13-16472

[11] S. Makita, Y.-J. Hong, M. Miura, and Y. Yasuno, "Degree of polarization uniformity with high noise immunity using polarization-sensitive optical coherence tomography," **Opt. Lett.**, vol. 39, no. 24, pp. 6783–6786, Dec. 2014. [Online]. Available: http://ol.osa.org/abstract.cfm?URI=ol-39-24-6783

[12] N. Lippok, M. Villiger, and B. E. Bouma, "Degree of polarization uniformity and depolarization index: unambiguous depolarization contrast for optical coherence tomography," **Opt. Lett.**, vol. 40, no. 17, pp. 3954–3957, Sep. 2015. [Online]. Available: http://www.osapublishing.org/abstract.cfm?uri= ol-40-17-3954

[13] M. Yamanari, S. Tsuda, T. Kokubun, K. Omodaka, N. Aizawa, Y. Yokoyama, S. Kunimatsu-Sanuki, K. Maruyama, and T. Nakazawa, "Estimation of Jones matrix, birefringence and entropy using Cloude-Pottier decomposition in polarization-sensitive optical coherence tomography," **Biomed. Opt. Express**, vol. 7, no. 9, pp. 3551–3573, Sep. 2016. [Online]. Available: https://www.osapublishing.org/boe/fulltext.cfm?uri=boe-7-9-3551&id=348934

[14] D. Kasaragod, S. Makita, Y.-J. Hong, and Y. Yasuno, "Noise stochastic corrected maximum a posteriori estimator for birefringence imaging using polarization-sensitive optical coherence tomography," **Biomed. Opt. Express**, vol. 8, no. 2, pp. 653–669, Feb. 2017. [Online]. Available: http: //www.osapublishing.org/abstract.cfm?uri=boe-8-2-653

[15] L. Duan, S. Makita, M. Yamanari, Y. Lim, and Y. Yasuno, "Monte-Carlo-based phase retardation estimator for polarization sensitive optical coherence tomography," **Opt. Express**, vol. 19, no. 17, pp. 16 330–16 345, Aug.

Bibliography (Continue)

2011. [Online]. Available: http://www.opticsexpress.org/abstract.cfm?URI=oe-19-17-16330

[16] L. Chin, A. Curatolo, B. F. Kennedy, B. J. Doyle, P. R. T. Munro, R. A. McLaughlin, and D. D. Sampson, "Analysis of image formation in optical coherence elastography using a multiphysics approach," **Biomed. Opt. Express**, vol. 5, no. 9, pp. 2913–2930, Sep. 2014. [Online]. Available: http://www.opticsinfobase.org/boe/abstract.cfm?URI=boe-5-9-2913

[17] P. R. Munro, A. Curatolo, and D. D. Sampson, "Full wave model of image formation in optical coherence tomography applicable to general samples," **Opt. Express**, vol. 23, no. 3, pp. 2541–2556, Feb. 2015. [Online]. Available: http://www.opticsexpress.org/abstract.cfm?URI=oe-23-3-2541

[18] Y. LeCun, Y. Bengio, and G. Hinton, "Deep learning," **Nature**, vol. 521, no. 7553, pp. 436–444, May 2015. [Online]. Available: http://www.nature.com/articles/nature14539

[19] M. M. Najafabadi, F. Villanustre, T. M. Khoshgoftaar, N. Seliya, R. Wald, and E. Muharemagic, "Deep learning applications and challenges in big data analytics," **J. Big Data**, vol. 2, no. 1, p. 1, Dec. 2015. [Online]. Available: https://journalofbigdata.springeropen.com/articles/10.1186/s40537-014-0007-7

[20] X. Sui, Y. Zheng, B. Wei, H. Bi, J. Wu, X. Pan, Y. Yin, and S. Zhang, "Choroid segmentation from optical coherence tomography with graph-edge weights learned from deep convolutional neural networks," **Neurocomputing**, vol. 237, pp. 332–341, May 2017. [Online]. Available: https://linkinghub.elsevier.com/retrieve/pii/S0925231217300541

[21] F. G. Venhuizen, B. van Ginneken, B. Liefers, M. J. van Grinsven, S. Fauser, C. Hoyng, T. Theelen, and C. I. Sánchez, "Robust total retina thickness segmentation in optical coherence tomography images using convolutional neural networks," **Biomed. Opt. Express**, vol. 8, no. 7, pp. 3292–3316, Jul. 2017. [Online]. Available: https://www.osapublishing.org/abstract.cfm?URI=boe-8-7-3292

[22] A. G. Roy, S. Conjeti, S. P. K. Karri, D. Sheet, A. Katouzian, C. Wachinger, and N. Navab, "ReLayNet: retinal layer and fluid segmentation of macular optical coherence tomography using fully convolutional networks," **Biomed. Opt. Express**, vol. 8, no. 8, pp. 3627–3642, Aug. 2017. [Online]. Available: https://www.osapublishing.org/abstract.cfm?URI=boe-8-8-3627

Bibliography (Continue)

[23] M. Pekala, N. Joshi, T. A. Liu, N. Bressler, D. C. DeBuc, and P. Burlina, "Deep learning based retinal OCT segmentation," **Comput. Biol. Med.**, vol. 114, p. 103445, Nov. 2019. [Online]. Available: https://linkinghub.elsevier.com/retrieve/pii/S0010482519303221

[24] C. S. Lee, A. J. Tyring, N. P. Deruyter, Y. Wu, A. Rokem, and A. Y. Lee, "Deep-learning based, automated segmentation of macular edema in optical coherence tomography," **Biomed. Opt. Express**, vol. 8, no. 7, pp. 3440–3448, Jul. 2017, publisher: Optical Society of America. [Online]. Available: https://www.osapublishing.org/boe/abstract.cfm?uri=boe-8-7-3440

[25] H. Mohsen, E.-S. A. El-Dahshan, E.-S. M. El-Horbaty, and A.-B. M. Salem, "Classification using deep learning neural networks for brain tumors," **Future Computing Inform. J.**, vol. 3, no. 1, pp. 68–71, Jun. 2018. [Online]. Available: https://linkinghub.elsevier.com/retrieve/pii/S2314728817300636

[26] Y. Ma, X. Chen, W. Zhu, X. Cheng, D. Xiang, and F. Shi, "Speckle noise reduction in optical coherence tomography images based on edge-sensitive cGAN," **Biomed. Opt. Express**, vol. 9, no. 11, pp. 5129–5146, Nov. 2018. [Online]. Available: https://www.osapublishing.org/abstract.cfm?URI=boe-9-11-5129

[27] S. K. Devalla, G. Subramanian, T. H. Pham, X. Wang, S. Perera, T. A. Tun, T. Aung, L. Schmetterer, A. H. Thiéry, and M. J. A. Girard, "A deep learning approach to denoise optical coherence tomography images of the optic nerve head," **Sci. Rep.**, vol. 9, no. 1, p. 14454, Dec. 2019. [Online]. Available: http://www.nature.com/articles/s41598-019-51062-7

[28] G. Litjens, T. Kooi, B. E. Bejnordi, A. A. A. Setio, F. Ciompi, M. Ghafoorian, J. A. van der Laak, B. van Ginneken, and C. I. Sánchez, "A survey on deep learning in medical image analysis," **Med. Image Anal.**, vol. 42, pp. 60–88, Dec. 2017. [Online]. Available: https://linkinghub.elsevier.com/retrieve/pii/S1361841517301135

[29] R. Yamashita, M. Nishio, R. K. G. Do, and K. Togashi, "Convolutional neural networks: an overview and application in radiology," **Insights Imaging**, vol. 9, no. 4, pp. 611–629, Aug. 2018. [Online]. Available: https://insightsimaging.springeropen.com/articles/10.1007/s13244-018-0639-9

[30] A. Khan, A. Sohail, U. Zahoora, and A. S. Qureshi, "A survey of the recent architectures of deep convolutional neural networks," **Artif. Intell.**

Bibliography (Continue)

Rev., vol. 53, no. 8, pp. 5455–5516, Dec. 2020. [Online]. Available: https://link.springer.com/10.1007/s10462-020-09825-6

[31] D. Huang, E. Swanson, C. Lin, J. Schuman, W. Stinson, W. Chang, M. Hee, T. Flotte, K. Gregory, C. Puliafito, and a. et, "Optical coherence tomography," **Science**, vol. 254, no. 5035, pp. 1178–1181, Nov. 1991. [Online]. Available: https://www.sciencemag.org/lookup/doi/10.1126/science.1957169

[32] N. Gonzalo, P. W. Serruys, T. Okamura, Z. J. Shen, Y. Onuma, H. M. Garcia-Garcia, G. Sarno, C. Schultz, R. J. van Geuns, J. Ligthart, and E. Regar, "Optical coherence tomography assessment of the acute effects of stent implantation on the vessel wall: a systematic quantitative approach," **Heart**, vol. 95, no. 23, pp. 1913–1919, Dec. 2009.

[33] I.-K. Jang, "In Vivo Characterization of Coronary Atherosclerotic Plaque by Use of Optical Coherence Tomography," **Circulation**, vol. 111, no. 12, pp. 1551–1555, Mar. 2005.

[34] Y. Ozaki, H. Kitabata, H. Tsujioka, S. Hosokawa, M. Kashiwagi, K. Ishibashi, K. Komukai, T. Tanimoto, Y. Ino, S. Takarada, T. Kubo, K. Kimura, A. Tanaka, K. Hirata, M. Mizukoshi, T. Imanishi, and T. Akasaka, "Comparison of Contrast Media and Low-Molecular-Weight Dextran for Frequency-Domain Optical Coherence Tomography," **Circulation Journal**, vol. 76, no. 4, pp. 922–927, 2012.

[35] F. Prati, E. Regar, G. S. Mintz, E. Arbustini, C. Di Mario, I.-K. Jang, T. Akasaka, M. Costa, G. Guagliumi, E. Grube, Y. Ozaki, F. Pinto, P. W. Serruys, and for the Expert's OCT Review Document, "Expert review document on methodology, terminology, and clinical applications of optical coherence tomography: physical principles, methodology of image acquisition, and clinical application for assessment of coronary arteries and atherosclerosis," **European Heart Journal**, vol. 31, no. 4, pp. 401–415, Feb. 2010.

[36] B. W. Colston, U. S. Sathyam, L. B. DaSilva, M. J. Everett, P. Stroeve, and L. L. Otis, "Dental oct," **Optics express**, vol. 3, no. 6, pp. 230–238, 1998.

[37] F. I. Feldchtein, G. V. Gelikonov, V. M. Gelikonov, R. R. Iksanov, R. V. Kuranov, A. M. Sergeev, N. D. Gladkova, M. N. Ourutina, J. A. Warren, and D. H. Reitze, "In vivo OCT imaging of hard and soft tissue of the oral cavity," **Optics Express**, vol. 3, no. 6, p. 239, Sep. 1998.

[38] V. Damodaran, S. R. Rao, and N. J. Vasa, "Optical coherence tomography based imaging of dental demineralisation and cavity restoration in 840nm and

Bibliography (Continue)

1310nm wavelength regions," **Optics and Lasers in Engineering**, vol. 83, pp. 59–65, Aug. 2016.

[39] J. Welzel, E. Lankenau, R. Birngruber, and R. Engelhardt, "Optical coherence tomography of the human skin," **Journal of the American Academy of Dermatology**, vol. 37, no. 6, pp. 958–963, 1997.

[40] M. Ulrich, T. von Braunmuehl, H. Kurzen, T. Dirschka, C. Kellner, E. Sattler, C. Berking, J. Welzel, and U. Reinhold, "The sensitivity and specificity of optical coherence tomography for the assisted diagnosis of nonpigmented basal cell carcinoma: an observational study," **British Journal of Dermatology**, vol. 173, no. 2, pp. 428–435, Aug. 2015.

[41] T. Gambichler, G. Moussa, M. Sand, D. Sand, P. Altmeyer, and K. Hoffmann, "Applications of optical coherence tomography in dermatology," **Journal of Dermatological Science**, vol. 40, no. 2, pp. 85–94, Nov. 2005.

[42] M. J. Gora, J. S. Sauk, R. W. Carruth, K. A. Gallagher, M. J. Suter, N. S. Nishioka, L. E. Kava, M. Rosenberg, B. E. Bouma, and G. J. Tearney, "Tethered capsule endomicroscopy enables less invasive imaging of gastrointestinal tract microstructure," **Nature Medicine**, vol. 19, no. 2, pp. 238–240, Jan. 2013.

[43] K. Kobayashi, J. A. Izatt, M. D. Kulkarni, J. Willis, and M. V. Sivak, "High-resolution cross-sectional imaging of the gastrointestinal tract using optical coherence tomography: preliminary results," **Gastrointestinal endoscopy**, vol. 47, no. 6, pp. 515–523, 1998.

[44] T.-H. Tsai, J. Fujimoto, and H. Mashimo, "Endoscopic Optical Coherence Tomography for Clinical Gastroenterology," **Diagnostics**, vol. 4, no. 2, pp. 57–93, May 2014.

[45] E. A. Swanson, J. A. Izatt, C. P. Lin, J. G. Fujimoto, J. S. Schuman, M. R. Hee, D. Huang, and C. A. Puliafito, "In vivo retinal imaging by optical coherence tomography," **Optics letters**, vol. 18, no. 21, pp. 1864–1866, 1993.

[46] A. F. Fercher, C. K. Hitzenberger, W. Drexler, G. Kamp, and H. Sattmann, "In Vivo Optical Coherence Tomography," **American Journal of Ophthalmology**, vol. 116, no. 1, pp. 113–114, Jul. 1993.

[47] A. F. Fercher, C. K. Hitzenberger, G. Kamp, and S. Y. El-Zaiat, "Measurement of intraocular distances by backscattering spectral interferometry," **Optics Communications**, vol. 117, no. 1, pp. 43–48, May 1995.

Bibliography (Continue)

[48] J. F. de Boer, B. Cense, B. H. Park, M. C. Pierce, G. J. Tearney, and B. E. Bouma, "Improved signal-to-noise ratio in spectral-domain compared with time-domain optical coherence tomography," **Optics Letters**, vol. 28, no. 21, p. 2067, Nov. 2003.

[49] M. A. Choma, M. V. Sarunic, C. Yang, and J. A. Izatt, "Sensitivity advantage of swept source and Fourier domain optical coherence tomography," **Optics express**, vol. 11, no. 18, pp. 2183–2189, 2003.

[50] R. Leitgeb, C. Hitzenberger, and A. Fercher, "Performance of fourier domain vs time domain optical coherence tomography," **Optics Express**, vol. 11, no. 8, p. 889, Apr. 2003.

[51] M. Wojtkowski, R. Leitgeb, A. Kowalczyk, T. Bajraszewski, and A. F. Fercher, "In vivo human retinal imaging by Fourier domain optical coherence tomography," **Journal of Biomedical Optics**, vol. 7, no. 3, p. 457, 2002.

[52] S. R. Chinn, E. A. Swanson, and J. G. Fujimoto, "Optical coherence tomography using a frequency-tunable optical source," **Optics Letters**, vol. 22, no. 5, p. 340, Mar. 1997.

[53] S. Yun, G. Tearney, J. de Boer, N. Iftimia, and B. Bouma, "High-speed optical frequency-domain imaging," **Optics express**, vol. 11, no. 22, pp. 2953–2963, 2003.

[54] G. E. Hinton, S. Osindero, and Y.-W. Teh, "A Fast Learning Algorithm for Deep Belief Nets," **Neural Computation**, vol. 18, no. 7, pp. 1527–1554, Jul. 2006. [Online]. Available: https://direct.mit.edu/neco/article/18/7/1527-1554/7065

[55] Y. Bengio, P. Lamblin, D. Popovici, and H. Larochelle, "Greedy Layer-Wise Training of Deep Networks," p. 8.

[56] D. P. Kingma and J. Ba, "Adam: A method for stochastic optimization," **arXiv:1412.6980 [cs]**, Jan. 2017, arXiv: 1412.6980. [Online]. Available: http://arxiv.org/abs/1412.6980

[57] B. W. Pogue and M. S. Patterson, "Review of tissue simulating phantoms for optical spectroscopy, imaging and dosimetry," **J. Biomed. Opt.**, vol. 11, no. 4, p. 041102, 2006. [Online]. Available: http://biomedicaloptics.spiedigitallibrary.org/article.aspx?doi=10.1117/1.2335429

Bibliography (Continue)

[58] X. Wen, V. V. Tuchin, Q. Luo, and D. Zhu, “Controling the scattering of Intralipid by using optical clearing agents,” **Phys. Med. Biol.**, vol. 54, no. 22, pp. 6917–6930, Nov. 2009. [Online]. Available: https://iopscience.iop.org/article/10.1088/0031-9155/54/22/011

[59] G. Zaccanti, S. Del Bianco, and F. Martelli, “Measurements of optical properties of high-density media,” **Appl. Opt.**, vol. 42, no. 19, pp. 4023–4030, Jul. 2003. [Online]. Available: https://www.osapublishing.org/abstract.cfm?URI=ao-42-19-4023

[60] R. Michels, F. Foschum, and A. Kienle, “Optical properties of fat emulsions,” **Opt. Express**, vol. 16, no. 8, pp. 5907–5925, Apr. 2008. [Online]. Available: https://www.osapublishing.org/oe/abstract.cfm?uri=oe-16-8-5907

[61] I. Abd El-Sadek, A. Miyazawa, L. Tzu-Wei Shen, S. Makita, S. Fukuda, T. Yamashita, Y. Oka, P. Mukherjee, S. Matsusaka, T. Oshika, H. Kano, and Y. Yasuno, “Optical coherence tomography-based tissue dynamics imaging for longitudinal and drug response evaluation of tumor spheroids,” **Biomed. Opt. Express**, vol. 11, no. 11, pp. 6231–6248, Nov. 2020. [Online]. Available: https://www.osapublishing.org/abstract.cfm?URI=boe-11-11-6231

[62] E. Li, S. Makita, Y.-J. Hong, D. Kasaragod, and Y. Yasuno, “Three-dimensional multi-contrast imaging of in vivo human skin by Jones matrix optical coherence tomography,” **Biomed. Opt. Express**, vol. 8, no. 3, pp. 1290–1305, Mar. 2017. [Online]. Available: https://www.osapublishing.org/abstract.cfm?URI=boe-8-3-1290

[63] M. J. Ju, Y.-J. Hong, S. Makita, Y. Lim, K. Kurokawa, L. Duan, M. Miura, S. Tang, and Y. Yasuno, “Advanced multi-contrast Jones matrix optical coherence tomography for Doppler and polarization sensitive imaging,” **Opt. Express**, vol. 21, no. 16, pp. 19 412–19 436, Aug. 2013. [Online]. Available: http://www.opticsexpress.org/abstract.cfm?URI=oe-21-16-19412

[64] J. G. Fujimoto and W. Drexler, “Introduction to OCT,” in **Optical Coherence Tomography: Technology and Applications**, W. Drexler and J. G. Fujimoto, Eds. Switzerland: Springer International Publishing, 2015, pp. 3–64. [Online]. Available: https://doi.org/10.1007/978-3-319-06419-2_1

[65] G. Farhat, A. Mariampillai, V. X. D. Yang, G. J. Czarnota, and M. C. Kolios, “Optical coherence tomography speckle decorrelation for detecting

Bibliography (Continue)

cell death," **Proc. SPIE**, p. 790710, Feb. 2011. [Online]. Available: http://proceedings.spiedigitallibrary.org/proceeding.aspx?doi=10.1117/12.874682

[66] T. van Leeuwen, D. Faber, and M. Aalders, "Measurement of the axial point spread function in scattering media using single-mode fiber-based optical coherence tomography," **IEEE Journal of Selected Topics in Quantum Electronics**, vol. 9, no. 2, pp. 227–233, 2003.

[67] B. Karamata, M. Laubscher, M. Leutenegger, S. Bourquin, T. Lasser, and P. Lambelet, "Multiple scattering in optical coherence tomography. i. investigation and modeling," **J. Opt. Soc. Am. A**, vol. 22, no. 7, pp. 1369–1379, Jul 2005. [Online]. Available: http://www.osapublishing.org/josaa/abstract.cfm?URI=josaa-22-7-1369

Biography

Thitiya Seesan was born in Nakhon Nayok, May 20, 1996. She graduated from Malasawan Phittaya school, high school, in 2013 and obtained her degree in Bachelor of Science in May 2017 from the Faculty of Science, King Mongkut's Institute of Technology Ladkrabang, Thailand. Her thesis is about developing a code for finite differences in time-domain (FDTD) methods for calculating and analyzing the phase velocity of light propagation at the boundary between the conventional material and metamaterial.

During and following her undergraduate career, Thitiya fulfilled knowledge in various optics fields, including optical coherence tomography and deep learning. In addition, she is a member of the Computational Optics Group, University of Tsukuba, Japan.

At the University of Tsukuba, she established a new tissue dynamics imaging modality, for multifunctional OCT microscopy, and publish it as a journal paper.